Materials Plus
https://ojs.wiserpub.com/index.php/MP/

Research Article

An investigation into the effect of anode platinum loading on Direct Methanol Fuel Cell performance

Thanarajan K.[1], Chen R.[2], Fly A.[3], Magesh Kannan V.[1], Karthikeyan. M.[1], Senthilarasu Sundaram[4], Karthikeyan P.[1*]

[1]Fuel Cells and Energy Systems Laboratory, Department of Automobile Engineering, PSG College of Technology, Coimbatore, 641004, India
[2]Department of Mechanical Engineering, Tianjin University, 135 Yaguan Road, Haihe Education Park, Jinnan District, Tianjin, China
[3]Department of Aeronautical and Automotive Engineering, Loughborough University, LE11 3TT UK
[4]School of Computing, Engineering and Digital Technologies, Teesside University, Tees Valley Middlesbrough, TS1 3BX, UK
E-mail: apk.auto@psgtech.ac.in

Received: 6 June 2024; **Accepted:** 6 June 2024

Abstract: Direct methanol fuel cells can utilize a liquid methanol fuel directly, without the need for prior reformation. This ability is highly advantageous when compared with other fuel cell technologies, which require pure hydrogen as a fuel source. An investigation was carried out to try and optimize the anode platinum loading using both Pt-$NiTiO_3$ and Pt-Ru based electrocatalysts by determining a point of diminishing performance returns. The results showed continued performance improvement as anode platinum loading increased for the Pt-$NiTiO_3$ catalyst, likely as a result of the methanol oxidation capabilities of $NiTiO_3$. Whereas, for Pt-Ru based catalysts, an optimum point was found at 0.66 $mg_{Pt}\,cm^{-2}$.

***Keywords*:** direct methanol fuel cell; anode electrocatalyst; Pt loading optimization; catalyst comparison

Nomenclature

Term	Description
DMFC	Direct Methanol Fuel Cell
GDL	Gas Diffusion Layer
GDE	Gas Diffusion Electrode
imax	Peak current density
IPA	IsoPropyl Alcohol
MEA	Membrane Electrode Assembly
MPL	MicroPorous Layer
$NiTiO_3$	Nickel Titanate
OCV	Open Circuit Voltage
PEMFC	Polymer Electrolyte Membrane Fuel Cell
Pt-$NiTiO_3$/C	Carbon supported Platinum Nickel Titanate

DOI: https://doi.org/10.37256/3220245105

1. Introduction

Direct methanol fuel cell (DMFC) technology [1,2] is one of the most promising power sources for portable applications due to the high theoretical energy density of methanol [3,4]. Also, Methanol is readily available throughout the world and is easy to distribute utilizing the present infrastructure for hydrocarbon fuels. Hence, DMFC are an exciting alternative to the ever-popular hydrogen-fuelled Polymer Electrolyte Membrane Fuel Cell (PEMFC) due to their ability to use a liquid methanol fuel directly, without the need for prior reformation. However, in the DMFC the anode catalyst itself draws the hydrogen from the liquid methanol, eliminating the need for a fuel reformer. The storage of hydrogen was eliminated because it is one of the major problems in PEMFCs.

Even though a DMFC has some advantages over hydrogen fuel cells, it also has some drawbacks for commercialization. DMFC technologies utilize platinum as the main catalyst component as it has been shown to outperform all other catalysts in the areas of activity, selectivity and stability for methanol oxidation-reduction [5]. So, by utilizing a rare material (platinum), the price of the catalyst was much higher; also, the electrocatalyst delivers low performance due to CO poisoning and crossover of methanol [6,7], lacking in reliability, sluggish kinetics for both methanol oxidation reaction [8,9] and oxygen reduction reaction [10,11]. To encounter catalyst poisoning due to the carbon monoxide produced during methanol decomposition in a DMFCs ruthenium co-catalyst is typically used [12]. At low temperatures, the CO molecules were adsorbed on the surfaces of the platinum catalyst [13,14]. In the meantime, at higher temperature methanol crossover is higher from anode to cathode due to the electro-osmatic drag.

These problems were rectified by developing a new catalyst to remove the CO molecules to CO_2 with a low percentage of rare/noble metals for cost-effectiveness. By increasing the thickness of the membrane and gas diffusion layer, methanol crossover and swelling of membrane were drastically reduced [15,16]. Also, high catalyst loadings are required to achieve reasonable performance and reduce the issues in DMFCs. Typically, anode catalyst loading in excess of 4.0 $mg_{Pt\text{-}Ru}\,cm^{-2}$ is favoured [17–20]. From the above literature, a new catalyst was required to catalyse the oxidation and reduction reaction, also to increase the rate of particular catalytic reaction [21]. Most of the research was focused on the selection and synthesis of materials to improve methanol oxidation reaction (MOR) [22–25] and to effectively promote the conversion of CO to CO_2. Hence the researchers found that ruthenium has the promotion capability of CO to CO_2 in DMFCs during the decomposition of methanol [26–28]. Still, the performance was poor and the electrocatalytic activity was low in DMFCs while using PtRu composites. Hence to overcome all these issues and to produce a cost-effective catalyst material for DMFCs, the researchers incorporate non-noble materials and metal oxides in the catalyst [29–38]. In that way, most of the research involved with experimentally investigated some metal oxides (TiO_2, IrO_2, CeO_2, V_2O_5, WO_x, MoO_3, $NiTiO_3$) as the co-catalyst to replace ruthenium to effectively oxidize methanol. Metal titanates are one of the common materials, referred as inorganic functional materials [39,40]. Nickel Titanate ($NiTiO_3$), in particular, is very interesting in the field of fuel cells due to its electrocatalytic properties and has been shown to oxidize methanol at 60 ℃ [40]. Montano et al.[41] explored Ni@Pt/RGO nanodisks for methanol electro-oxidation in alkaline media, revealing enhanced CO tolerance and improved performance towards MOR through the bifunctional effect and electronic interaction between Pt and Ni species. Amin et al. [42] demonstrated that the impregnation-prepared Pd-Ni/C electrocatalyst exhibited 1.92 and 1.68 times higher current density compared to Pd/C and Ni/C catalysts. $NiTiO_3$, with an ilmenite structure and octahedral coordination of Ni and Ti, has been evaluated for photocatalytic degradation of nitrobenzene and methylene blue in visible light. However, its potential application in fuel cells remains unexplored. Manoharan and Goodenough previously showed that a passivated oxide layer (<2 nm) on an ordered NiTi alloy catalyzed MOR in fuel cells [43]. Our recent work investigated Pt-$NiTiO_3$/C as an effective cathode catalyst for ORR, yet $NiTiO_3$'s suitability as a DMFC anode catalyst has not been reported to the author's knowledge. Hence the activity of NiTiO3 on anode cocatalyst was described by Thiagarajan et al. [38]. However, in Nickel Titanate, the poisonous CO was converted to CO_2 because the TiO_2 improves the adsorption of OH species. In our previous work, we proved that the addition of $NiTiO_3$ with Pt/C promotes the methanol oxidation reaction activity and durability of the catalyst.

Manufacturing of nickel titanate nanoparticles by wet-chemical synthesis has been widely discussed [39,44–47]. The usage of carbon-supported Platinum Nickel Titanate (Pt-$NiTiO_3$/C) as an anode electrocatalyst in DMFCs has been previously suggested Thiagarajan et al. [38,44,45]. Peak deliverable fuel cell power was found to increase by 16.7% by changing the anode catalyst from Pt-Ru/C to Pt-$NiTiO_3$/C [44]. The utilization of $NiTiO_3$ is further justified as the efficiency of ruthenium containing catalysts is thought to decrease over time due to the leaching of ruthenium while potential cycling [40,46–49].

In this work, the platinum loading on anode catalyst for DMFC was optimized on Pt-$NiTiO_3$/C based electrocatalyst. This will avoid a case of diminishing performance returns and help to optimize the

cost/performance ratio. The main aim of the novel electrocatalyst was to reduce the fuel cell cost by allowing a smaller quantity of expensive precious metals, such as platinum and ruthenium, to be utilized without a fall in performance [44].

2. Materials and methods

2.1 *Chemicals and reagents*

The following reagents and chemicals, dihydrogen hexachloroplatinate (IV) hexahydrate ($H_2PtCl_6.6H_2O$) (Johnson Matthey, UK), Methanol (Merck, India) (99.6% Purity), isopropanol (Hi-Media), KOH (Merck, India), nickel acetate (Loba Chemie, India) and titanium(IV) Isopropoxide and citric Acid (Aldrich, USA) are of analytical grade and used as received. Vulcan carbon XC-72 has been received from M/s Cabot Corp. and 5 wt. % Nafion ionomer has been received from DuPont (USA). All the solutions used for the experiments have been prepared with ultrapure water with resistivity of 18.2 MΩ cm. All glass apparatus have been cleaned with chromic acid, washed with double distilled water, rinsed with acetone (Merck) and dried.

2.2 *Synthesis of Pt-NiTiO3/C catalysts*

Pt-$NiTiO_3$/C nanoparticles were synthesized by wet-chemical method. Initially, the $NiTiO_3$ nanoparticles were synthesized with a stoichiometric ratio of 1:1 Ni:Ti (nickel acetate and titanium (IV) isopropoxide) and it was liquified in methanol solution individually. In the titanium isopropoxide solution, the desired mass of Vulcan carbon XC-72 was added and stirred. In the nickel acetate solution, citric acid with 1.5 times the concentration of Ni^{2+} was added and stirred. Later the solution was heated at 90 ℃ for 12 hours to remove the excess solvent. Then the gained powdered material was calcinated at 700 ℃ for 3 hours in the Argon atmosphere. On the other hand, the chloroplatinic acid hexahydrate was dispersed in water-isopropanol solution. Now the Pt (40 wt. %) $NiTiO_3$ /C was prepared by combining the $NiTiO_3$/c with water-isopropanol dispersed chloroplatinic acid. To fix the pH of the solution at 7, 0.2 M Na_2CO_3 was added. Also, 0.2 M of $NaBH_4$ solution was additionally added to reduce the prepared solution. After that, the prepared mixture was heated at 70 ℃ and the solution was filtered. The obtained catalyst powder was dried in a vacuum oven at 80℃ overnight. Finally, the required stoichiometric ratio of 40 wt. % Pt 20 wt. % $NiTiO_3$ 40 wt. % C nanocomposite material was obtained [48]. The schematic diagram is shown in Fig. 1.

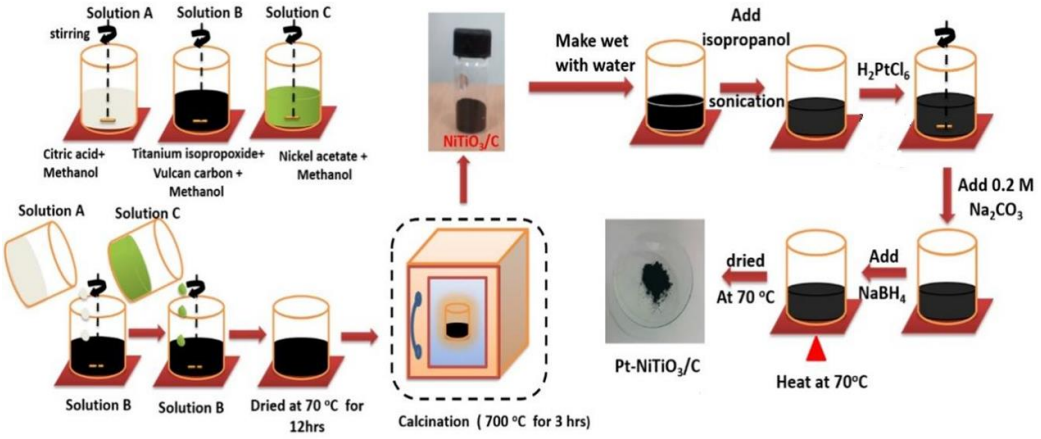

Figure 1. Schematic representation for the synthesis of Pt-$NiTiO_3$/C

2.3 *Materials characterization*

Pt-$NiTiO_3$/C and Pt/C catalysts have been characterized by XRD using Philips X-ray diffractometer with Cu Kα radiation source. JEOL JEM 2100 with an operating voltage of 200 kV (manufactured in Japan) has been used for recording the TEM images. X-ray Photoelectron Spectroscopy (XPS) measurements have been carried out using a PHI-5702 multifunctional OMICRON NANOTECHNOLOGY, (Germany) X-ray photoelectron spectrometer with Al Kα radiation (hύ = 1486.6 eV). The XPS peaks are deconvoluted using XPS peak fit V4 software and the binding energy values are compared from the XPS database present in Lasurface.com.

3. Cell Fabrication

A Membrane Electrode Assembly (MEA) typically consists of seven layers: two Gas Diffusion Layers (GDL), two Microporous Layers (MPL), two catalyst layers and a membrane. The arrangement of these layers in a complete MEA is shown in Fig. 2. It is also common practice to refer to the sub-assembly of GDL, MPL and catalyst layer as a Gas Diffusion Electrode (GDE).

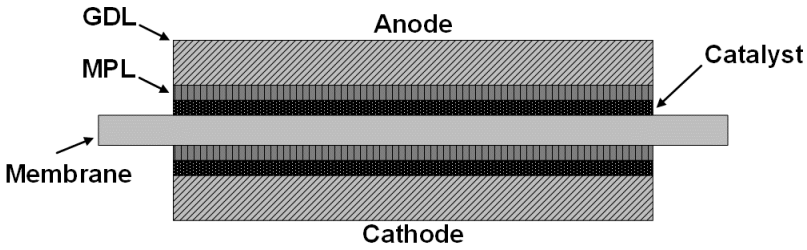

Figure 2. Arrangement of a seven-layer membrane electrode assembly

3.1 *Catalyst ink preparation*

Anode catalyst inks were prepared using Pt-$NiTiO_3$/C novel catalyst powder, manufactured using the wet chemical method developed by Thiagarajan et al. [45], with a mass breakdown of 40% platinum, 20% $NiTiO_3$ and 40% carbon support, water-based D1021 Nafion™ ionomer dispersion and Isopropyl Alcohol (IPA) ≥99.7% as solvent. Appropriate quantities of each of the catalyst ink constituents, as defined in Table 1 were measured and added to a mixing vial in the following order to avoid ignition of the platinum-based catalyst powder: Catalyst powder → Ionomer → Solvent.

Table 1. Mass fraction of constituents in wet catalyst ink mixture

Constituent	Percentage of total wet ink mixture by mass
Catalyst powder	3%
Ionomer	40%
Solvent – IPA	57%

The ink mixture was swirled by hand after the addition of the ionomer and before the addition of the IPA to ensure that all the catalyst powder had been wetted. The mixture was then sonicated for 120 mins using a camlab camSonix C175 digital ultrasound bath at a frequency of 37 kHz to ensure a colloidal suspension. The sonication time was based on a literature survey where two hours was found to be typical [50,51].

3.2 *Catalyst ink coating*

Catalyst ink was coated onto CeTech carbon cloth with microporous layer GDL (FuelCellStore.com 1595000) using a bar coater at a speed of 1.0 mm s^{-1}. To ensure consistency between the different coatings, the coating was carried out in a single layer. The single-layer coating is also beneficial from a mass manufacturing perspective as it helps to simplify the process. The coating Wet-Layer Thickness (WLT) defined by Equation I, was used to obtain different platinum loadings, where ρ_{Pt} is the area density of platinum, commonly given in mg cm^{-2}.

$$WLT = \frac{Target\ Pt\ loading\ \times\ Ink\ volume}{m_{Pt}} \quad \text{(I)}$$

An oversized section of GDL was used for each coating so that the uniformly coated middle section could be used in the assembly of the MEA. After coating, the catalyst ink mixture was allowed to dry for a minimum of 24 hours in ambient conditions. Once fully dry, the correct active area of GDE was cut out and its mass was measured. The difference in area density between the coated GDE (ρ_{GDE}) and uncoated GDL (ρ_{GDL}) was used to find the final platinum loading using Equation II.

$$Actual\ Pt\ loading = (\rho_{GDE} - \rho_{GDL}) \times \%Pt_{dry\ mix} \quad \text{(II)}$$

Where the percentage of platinum in the dry mix is defined by Equation III.

$$\%Pt_{dry\ mix} = \frac{\rho_{Pt}}{\rho_{catalyst\ powder} + \rho m_{dry\ ionomer}} \quad \text{(III)}$$

The mass of dry ionomer was calculated using the "equivalent dry density," which was deduced experimentally. This was done by pipetting a known quantity of Nafion™ D1021 Dispersion liquid into a vial, allowing it to dry naturally and weighing the remaining solid.

3.3 *Final assembly*

Coated anode GDEs were hot-pressed at a temperature of 120℃ for 180 seconds with Nafion™ 117 (FuelCellStore.com 591239) and a commercially purchased cathode GDE with a catalyst loading of 0.5 mg cm^{-2} 60 wt. % Pt/C (FuelCellStore.com 1610004). The pressure applied for hot pressing the GDE's to the membrane was 5MPa and 50MPa for the 25cm^2 and 100cm^2 MEA's respectively. The same cathode GDE was used for all MEAs to ensure that the main factor affecting fuel cell performance was the anode platinum loading. The final active area was 25cm^2 for the first stage of testing (MEA's 1–8) and 100cm^2 for the second stage of testing which involved single cell and 3-cell stack testing. Completed MEAs were installed into a Scribner Liquid-Gas Fuel Cell Fixture. The clamping pressure of the fuel cell bolts were tightened to 3Nm and 8Nm for the 25cm^2 and 100cm^2 cells respectively.

4. Testing Procedure

Four 25cm^2 MEAs were fabricated (MEA's 1-4) using the process outlined above. The maximum platinum loading achievable using the materials and its process outlined above was 0.66 mg_{Pt} cm^{-2} equivalent to a catalyst loading of 1.0 mg cm^{-2} Pt-$NiTiO_3$/C. For a comparison, four 25cm^2 commercial MEAs (MEA's 5-8) with various loadings of the more traditional Pt-Ru catalyst was obtained from the FuelCellStore.com. Four 100cm^2 MEAs were fabricated with a catalyst loading of 0.5 mg cm^{-2} Pt-$NiTiO_3$/C equivalent to 0.33 mg_{Pt} cm^{-2}. As a comparison, five 100cm^2 commercial MEA's were fabricated with various loadings of the more traditional Pt-Ru catalyst. These are listed in Table 2.

Table 2. List of MEAs used in experiments, all loadings given in mg cm^{-2}

MEA	25cm^2 MEA		MEA	100cm^2 MEA	
	Catalyst Loading (mg)	Platinum Loading (mg)		Catalyst Loading (mg)	Platinum Loading (mg)
1	0.44 (Pt-$NiTiO_3$)	0.29	**9**	2.0 (Pt-Ru)	1.32
2	0.62 (Pt-$NiTiO_3$)	0.41	**10**	4.0 (Pt-Ru)	2.64
3	0.99 (Pt-$NiTiO_3$)	0.65	**11**	0.5 (Pt-$NiTiO_3$)	0.33
4	1.0 (Pt-$NiTiO_3$)	0.66	**12 – 14 3 cell stack**	2.0 (Pt-Ru)	1.32
5	0.20 (Pt-Ru)	0.13	**15 – 17 3 cell stack**	0.5 (Pt-$NiTiO_3$)	0.33
6	0.50 (Pt-Ru)	0.33			
7	1.0 (Pt-Ru)	0.66			
8	2.0 (Pt-Ru)	1.32			

Each MEA was conditioned before performance evaluation. The same procedure for both conditioning and performance evaluation was used for each MEA to ensure consistency. Standard conditions for testing (both conditioning and performance evaluation) are shown in Table 3.

Table 3. Standard testing conditions

Parameter		Value
Anode flow	Methanol concentration	1.0 M
	Flow rate	3.0 ml min^{-1}
	Temperature	60 °C
Cathode flow	Reactant	Air
	Flow rate	500 ml min^{-1}
	Temperature	60 °C
	Humidity	100% RH
Other	Cell fixture temperature	60 °C

4.1 *Conditioning*

Conditioning, also known as "activation," is considered to play an important role in achieving the best DMFC performance possible [52]. The protocol outlined in Table 4 was used to activate the MEAs.

Table 4. Conditioning protocol for single cell DMFC

Step	Setpoint (mA cm^{-2})	Time (s)	Step	Setpoint (mA cm^{-2})	Time (s)
1	0	300	6	20	300
2	4	300	7	30	300
3	8	300	8	40	300
4	12	300	9	0	300
5	16	300	10	Polarization (OCV – 0.1V)	

The conditioning protocol was followed multiple times over several days for each fuel cell. An MEA was considered fully conditioned when the peak power increased by less than 5% between consecutive conditioning runs. This typically took 8-10 conditioning runs per MEA.

5. Results and discussion

5.1 *Performance evaluation on 25cm^2 MEA*

The X-ray diffractions (XRD) of Pt-$NiTiO_3$/C (Homemade) and Pt/C (Commercial) catalysts are shown in Fig. 3 (a).

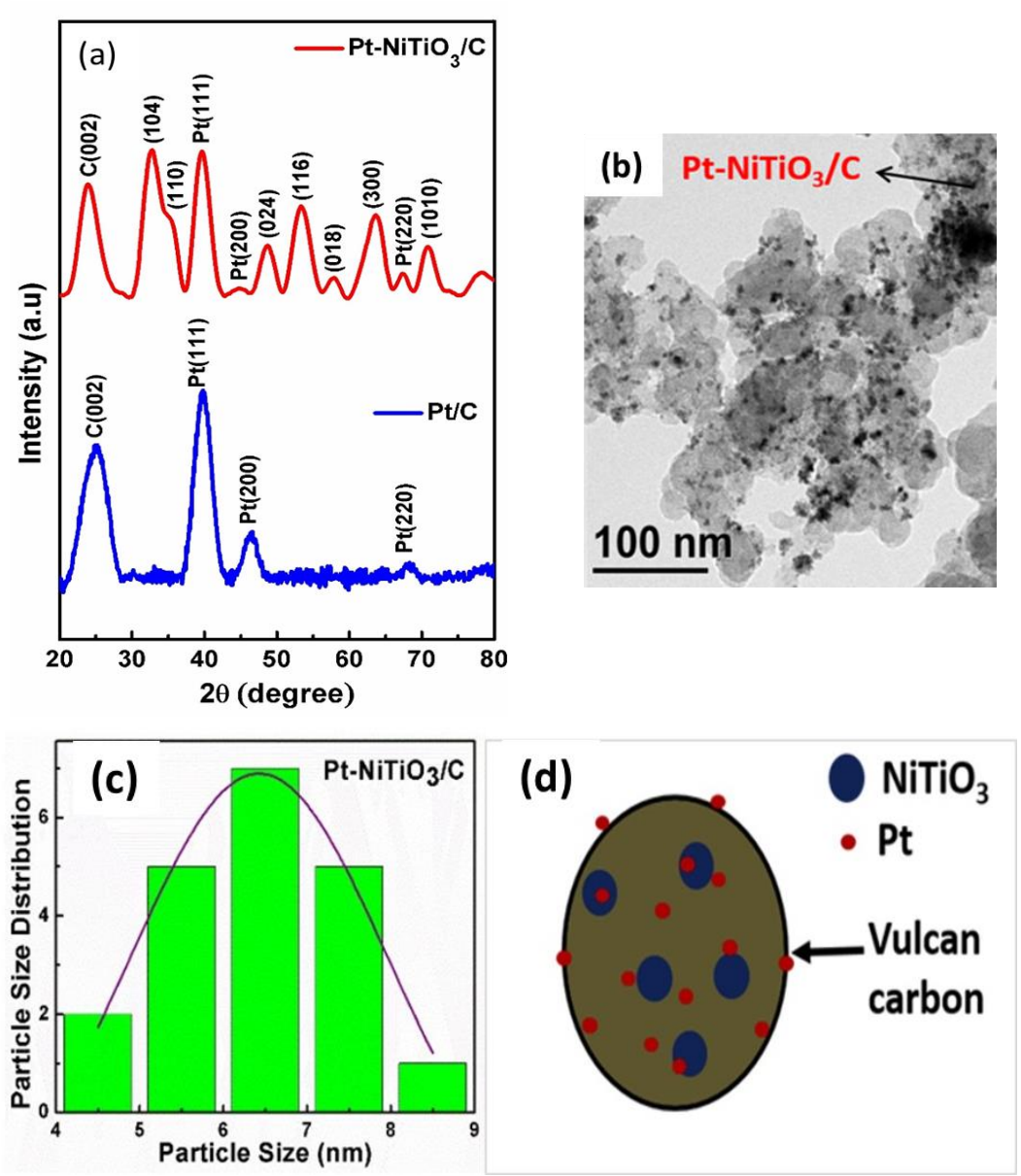

Figure 3. (a) XRD patterns of Pt/C and Pt-$NiTiO_3$/C catalysts (b) TEM image of Pt-$NiTiO_3$/C (c) Particle distribution of Pt-$NiTiO_3$/C and (d) schematic depiction of Pt distribution on $NiTiO_3$/C

In Fig. 3 (a), an extensive peak for carbon was observed at the 2 θ value of about 25°. It clearly indicates the pattern of Pt-$NiTiO_3$/C. The crystal size of prepared oxide was increased when it will be supported on Vulcan carbon and it was shown in the expansive peak's existence of $NiTiO_3$. The $NiTiO_3$ (104), (110), (024), (116), (018), (300), (1010) peaks were shown in the pattern of Pt dispersed on $NiTiO_3$/C. From the three X-ray diffraction peaks, about 2 θ (40°, 46.5°, 68.1°), the Pt crystal planes of (111), (200) and (220) were identified. The JCPDS ID 04-802 confirms that, the crystalline of Pt has the characteristics of face-centered cubic (FCC). Fig. 3 (b) shows the TEM images of Pt-$NiTiO_3$ nanoparticles dispersed on carbon. From the Debye-Scherrer formula, the average size of Pt-$NiTiO_3$/C nanoparticles was 4.6 nm, and it was calculated from Pt (111) crystalline plane using Fig. 3 (c). In general, there is a homogeneous distribution of Pt particles with some agglomeration, which has the characteristic of oxide incorporated samples. The even distribution of Pt-$NiTiO_3$ nanoparticles was attained by ultrasonication of the electrocatalyst. The different distribution in platinum size will affect the activity of catalyst. Fig. 4 shows the cyclic voltammetry of Pt-$NiTiO_3$/C by inducing methanol in acid and alkali solutions.

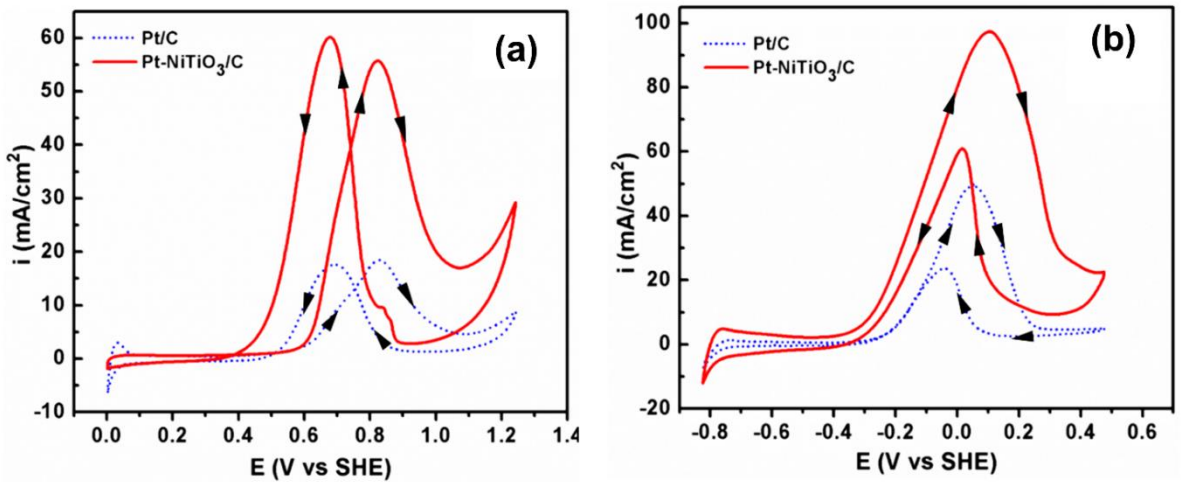

Figure 4. CVs for $NiTiO_3$/C with and without methanol in (a) 1 M CH_3OH/1 M H_2SO_4 solution and (b) 1 M CH_3OH / 0.5 M KOH solution

During the forward and backward scanning, the methanol oxidation peaks appeared because of the presence of electrochemical oxidation in methanol. Fig. 4 (a) and (b) shows the average current density, where the experiments were repeated for ten consecutive times. The maximum current density of Pt-$NiTiO_3$/C was achieved as 60 and 98 $mAcm^{-2}$ in acid and alkali media, respectively. The Cyclic voltammetry values have been recorded at a scan rate of 20 mV s^{-1}. The homemade catalyst performed better that the commercial catalyst and it was clearly shown in the Fig. 4. It is due to the combined effect of Pt with $NiTiO_3$ electrode and it will help to effectively remove the adsorbed CO on Pt sites. From the enhanced performance, it clearly shows that $NiTiO_3$ has the ability to remove CO species form the Pt sites using active oxygen.

The electrochemical stability of electrocatalyst was studied at room temperature for 20 minutes by using the chronoamperometry techniques at 0.84 V at acid media and 0.22 V at alkali media vs. SHE. The catalyst with Pt-$NiTiO_3$/C has a higher initial and limiting current densities than the Pt/C catalyst, which shows higher electrochemical activity and stability. This is due to the effective conversion of CO to CO_2 adsorbed on the surface of Pt. In the Pt-$NiTiO_3$/C electrocatalyst, $NiTiO_3$ was works like a cocatalyst and helps to remove the adsorbed CO species on the Pt sites, hence the CO poison tolerance of the electrocatalyst was improved. The results are shown in Fig. 5.

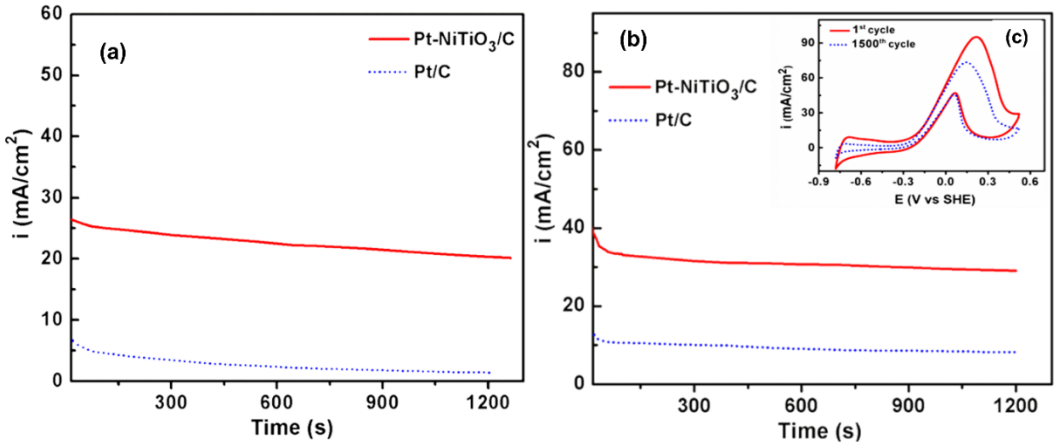

Figure 5. CA curves for the MOR on the catalysts Pt/C and Pt-$NiTiO_3$/C in (a) 0.5 M CH_3OH /1 M H_2SO_4 solution and (b) 1 M CH_3OH / 0.5 M KOH solution (c) Inset of CVs for Pt-$NiTiO_3$/C after 1500^{th} cycles

In Fig. 5(c) the CV of Pt-$NiTiO_3$/C catalyst's 1^{st} and 1500^{th} cycle was shown. Even after 1500 CV cycles, the catalyst has delivered 80 % of its initial performance. And it shows the stability of the electrocatalyst towards methanol oxidation reaction. However, the activation losses have been observed after 1500 CV cycles and it is due to the peel off catalyst from the electrode surface.

Fig. 6 shows the XPS analysis of Platinum electrocatalyst.

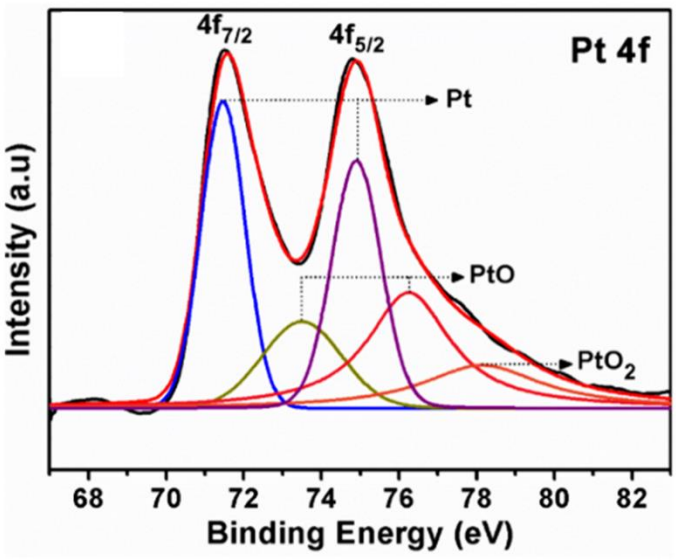

Figure 6. Core XPS spectra of Pt 4f

From the Fig. 6 4f region, two uneven peaks were found in the XPS core level energy spectrum of Pt. The platinum peaks at minimum and maximum binding energy of Pt were 71.5 eV at $4f_{7/2}$ and 74.9 eV at $4f_{5/2}$. Other Pt peaks were found that the binding energies of 73.5, 76.2 and 78.14 eV, which were allotted to Pt (II) and (IV) species.

The specialty of $NiTiO_3$ was to absorb the active oxygen from the aqueous electrolyte and it helps to convert the CO species to CO_2. The detailed studies of Pt-$NiTiO_3$/C material characterization and reactions mechanism equations (4) and (5) were proposed in our previous work [38].

$$NiTiO_3 + H_2O \rightarrow NiTiO_{3-x}(OH) + H^+ + e^- \quad (4)$$

$$Pt–CO_{ads} + NiTiO_{3-x}(OH) \rightarrow Pt + NiTiO_{3-x} + CO^2 + H^+ + e^- \quad (5)$$

5.1.1 *Polarization*

Fuel cell performance was evaluated by holding Open Circuit Voltage (OCV) for 300 seconds to check stability and then running an extended polarization curve with scan rate of 0.5 mVs^{-1} to ensure a pseudo steady-state. Polarization results for MEA 1 and MEA 4 are shown in Fig. 7. Low (0.29 mg_{Pt} cm^{-2}) and high (0.66 mg_{Pt} cm^{-2}) platinum loadings were chosen to represent the spread of data and highlight the extreme performance change from increasing the anode platinum loading.

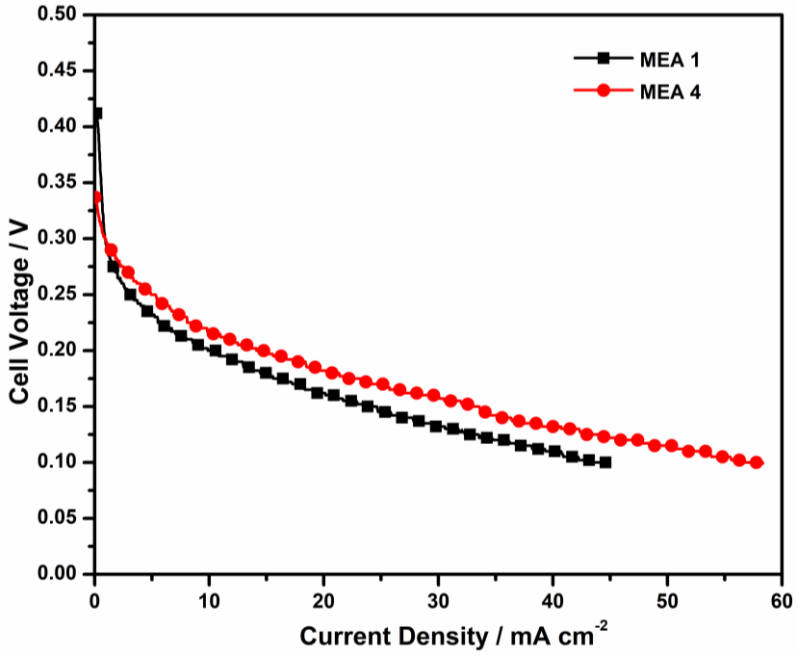

Figure 7. Conditioned polarization results for Pt-$NiTiO_3$/C 25cm^2 MEA's

The first stage in assessing the performance of the fuel cells was to evaluate the polarization results against the following three criteria: activation loss, ohmic resistance and peak current density.

Activation loss is the initial voltage drop as the current is drawn. This is of particular interest with DMFCs due to the relatively large amount of internal fuel crossover, which is prevalent in this type of fuel cell [20,52,53]. Fig. 7 shows that the activation loss associated with the Pt-$NiTiO_3$/C MEAs are not related to the change in anode platinum loading.

Ohmic loss is the voltage degradation due to internal electrical and ionic resistances. As all of the MEAs are tested in the same cell fixture and the GDL material is kept constant, the difference in gradient of the ohmic region of the polarization curves can be attributed to the differences in catalyst composition. The results show that ohmic losses are reduced as the anode platinum loading is increased, most likely as a result of lower electrode resistance form a higher metal/carbon ratio in the catalyst layer. Peak current density (i_{max}) is the maximum current achieved by each MEA. This typically occurs at the lowest cell potential, so it is not always the most suitable parameter by which to judge fuel cell performance. However, the results do show a 32% increase in i_{max} between the lowest and highest anode platinum loading MEAs.

5.1.2 *Peak power*

To enable a fair comparison of the effect of anode platinum loading on peak power between different catalyst compositions, the data has been normalized. This was done by defining the maximum peak power for each catalyst type individually and then ranking the MEAs in each group accordingly. The results of this analysis can be seen in **Error! Reference source not found.**.

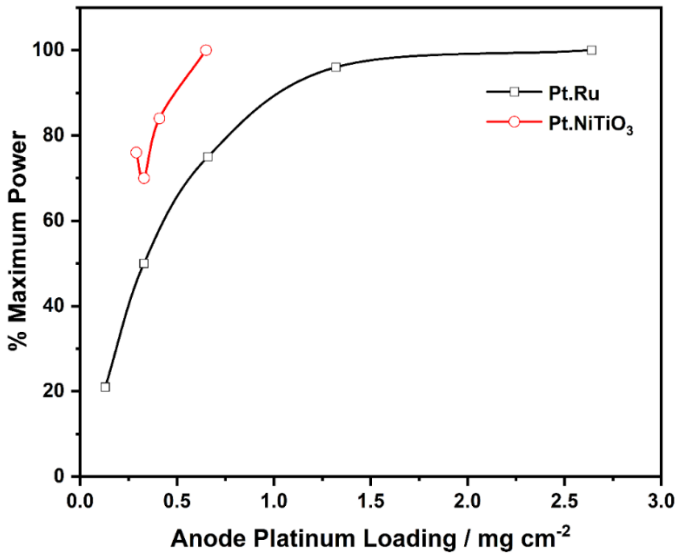

Figure 8. Variation of maximum power for each catalyst type with anode platinum loading

For the Pt-$NiTiO_3$ based MEAs the results show a general trend of increased maximum power as a function of increased anode platinum loading. The maximum power was achieved at a platinum loading of 0.65 mg_{Pt} cm^{-2}. As the anode platinum loading was increased from 0.29→0.41 mg_{Pt} cm^{-2}, the peak power increased at a rate of 34% per unit platinum loading. The increase rate was 64% per unit platinum loading as the anode platinum loading was increased from 0.41→0.65 mg_{Pt} cm^{-2}. These results were obtained from the 25 cm^{-2} MEAs. While, there is a slight drop in maximum power achieved at a platinum loading of 0.33 mg_{Pt} cm^{-2} was measured for the 100 cm^{-2} MEA. This could indicate that the coating technique needs to be optimised for large scale MEAs.

As the rate of increase in peak power continued to grow as the anode platinum loading from Pt-$NiTiO_3$ increased, it would be desirable to utilize a high catalyst loading with this electrocatalyst. The catalyst ink coating technique detailed in this paper was not capable of producing higher loadings whilst maintaining a uniform catalyst layer. Alternative coating techniques should be investigated to ensure the trend of exponentially increasing performance continues at higher anode platinum loadings.

Similar observations were identified for the traditional Pt-Ru based MEAs, where results showed a general relationship of increased maximum power as a function of increased anode platinum loading. Conversely,

however, the gradients of the relationships were reversed. The peak power increased at a rate of 149% per unit platinum loading as the anode platinum loading was increased from 0.13→0.33 mg_{Pt} cm^{-2}. The increase rate decreased to 79% per unit platinum loading as the anode platinum loading was increased from 0.33→0.66 mg_{Pt} cm^{-2}. The final increase rate was 33% per unit platinum loading as the anode platinum loading was increased from 0.66→1.32 mg_{Pt} cm^{-2}.

This trend of diminishing returns for performance of Pt-Ru based MEAs suggests that an optimum cost/performance ratio for this catalyst composition should be in the region of 0.66 mg_{Pt} cm^{-2}. As the Pt-Ru electrocatalyst used had platinum and ruthenium in a 1:1 atomic ratio, this equates to a 1.0 $mg_{Pt\text{-}Ru}$ cm^{-2} anode GDE. This is 25% of the current standard from literature, which typically suggests an excess of 4.0 $mg_{Pt\text{-}Ru}$ cm^{-2} is favoured [17–20].

5.2 *100cm² MEA*

5.2.1 *Test conditions*

Table 5 outlines the conditions used for testing the 100cm² MEAs.

Table 5. Testing conditions for 100cm² MEAs

Parameter		Value
Anode flow	Methanol concentration	1.0 M
	Flow rate	6 ml min^{-1}
	Temperature	40 °C
Cathode flow	Reactant	Air
	Flow rate	1500 ml min^{-1}
	Temperature	60 °C
	Humidity	100% RH
Other	Cell temperature	60 °C

5.2.2 *Polarization*

In the second stage of testing, 100cm² MEAs were fabricated in order to investigate the feasibility of the coating technique and performance of Pt-$NiTiO_3$/C catalyst for large scale MEA's.

shows the polarization results from 100cm² MEA's.

As expected, it is clear from the results that the 4mg Pt-Ru MEA produced the best performance, achieving the highest OCV and peak current density. Comparing the commercial Pt-Ru MEAs, a decrease in OCV of 0.28V (41%) was measured when comparing the 4.0 $mg_{Pt\text{-}Ru}$ cm^{-2} MEA with the 2.0 $mg_{Pt\text{-}Ru}$ cm^{-2} MEA. This decrease in OCV of 41% shows that the activation losses are associated with the 50% decrease in catalyst loading. In the ohmic region, there is also a significant difference in voltage. However, there is no increase in the voltage difference and the gradient of the curves does not change proportionally to the current applied which indicates that the internal electrical and ionic resistances are not a substantial factor. This suggests the main cause of the voltage difference is due to the lower catalyst loading.

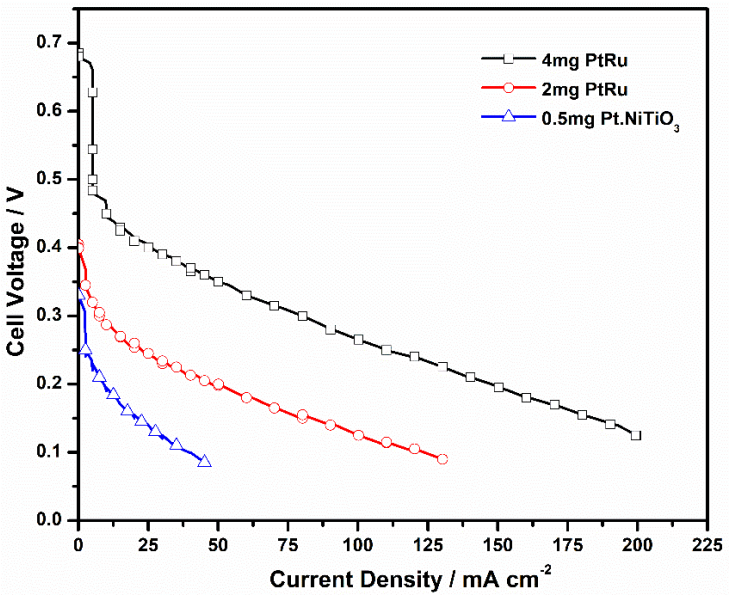

Figure 9. Conditioned polarization results for 100cm^2 MEA's

Comparing the 2mg Pt-Ru MEA with the 0.5mg Pt-$NiTiO_3$/C MEA, the decrease in OCV was measured at 0.07V (16.7%), In the activation region, the gradient of the curves from OCV to 10mA/cm^2 were 0.0116 and 0.0125 for the Pt-Ru and Pt-$NiTiO_3$/C MEAs respectively. The difference in OCV and the similarity in the gradient of the curves in the activation region shoes that the difference in voltage is again due to the difference in catalyst loading. The limited peak current density at 45 mA/cm^2 suggests that the low catalyst loading inhibits performance at higher current densities. The next important feature to compare is the peak power achieved by the MEAs.

5.2.3 *Peak power*

From the polarisation curves, peak power was also characterised. This characterises the maximum power achieved and demonstrates a more useful capability for DMFC operation. Fig. 10 shows the power density curves.

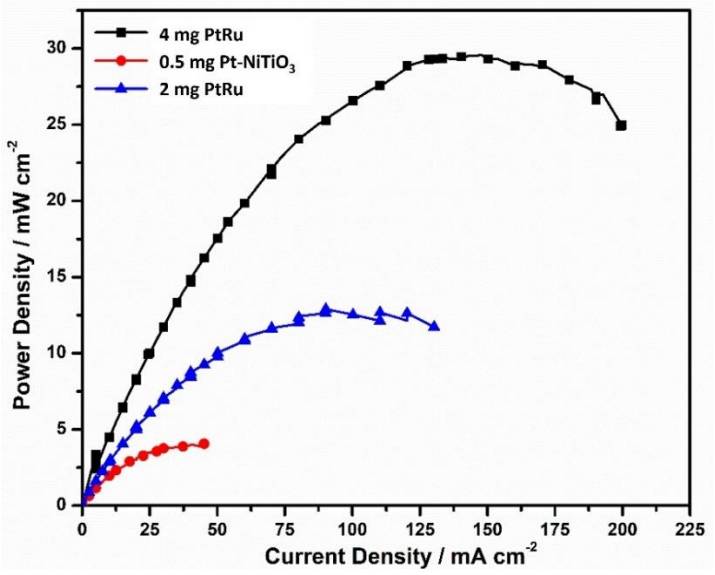

Figure 10. Power density curves for 100cm^2 Active area DMFC

As anticipated, the peak power density was achieved by the 4mg Pt-Ru MEA. Comparing the 4.0 $mg_{Pt\text{-}Ru}$ cm^{-2} MEA with the 2.0 $mg_{Pt\text{-}Ru}$ cm^{-2} MEA, a decrease in peak power density of 16.8 $mWcm^{-2}$ (56.9%) was measured. Comparing the 2mg Pt-Ru MEA with the 0.5mg Pt-$NiTiO_3$/C MEA, a decrease in peak power density of 8.4 $mWcm^{-2}$ (66.3%) was measured. This decrease of 66.3% in peak power density could be expected this is relative to the decrease in catalyst loading of 75%.

Overall, the results show that although the performance of the Pt-$NiTiO_3$/C MEA was limited, there is potential for improving the performance by increasing the catalyst loading up to 1.0 mg cm^{-2} or even 2.0 mg cm^{-2}. This would also enable more accurate performance comparison of MEAs with equal catalyst loadings. However, simply increasing the catalyst loading+

+-+96 is not the most cost effective method for improving performance so further experimental work would be required to identify the optimal catalyst loading in terms of both performance and cost.

5.2.4 *Stability test*

In an application, real DMFC performance will require the capability to operate or maintain a current demand over a set duration. In order to characterise this capability, a short-term stability test was conducted by applying a constant current of 1A for a duration of approx. 2hrs. Fig. 11 shows the stability test results.

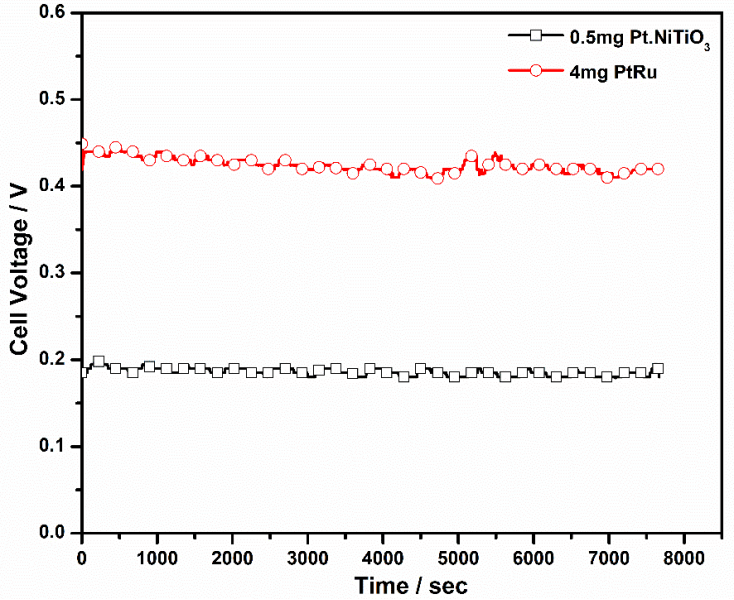

Figure 11. Short-term stability test for 100cm^2 MEA's

The results show that the Pt-Ru MEA maintained a voltage of 0.465V to 0.415V from start to finish and the Pt-$NiTiO_3$ MEA was able to maintain a voltage of 0.185V to 0.18V from start to finish. Over the duration of the test, the voltage degradation rates were calculated to be 23.5 mV/hr and 2.3 mV/hr for the 4mg Pt-Ru MEA and 0.5 mg Pt-$NiTiO_3$ MEA respectively. Although the Pt-Ru MEA was able to achieve a higher voltage due to the higher catalyst loading, the Pt-$NiTiO_3$ MEA showed greater stability over the 2hr test. The improved stability of the Pt-$NiTiO_3$ MEA is because the $NiTiO_3$ improves the efficiency of CO conversion to CO_2 and the Ni enables improved proton transfer rate. The improved stability of the Pt-$NiTiO_3$ MEA provides promising results. Further testing should investigate the stability of the Pt-$NiTiO_3$ for longer durations and stability of higher catalyst loadings.

5.2.5 *Scanning electron microscopy and energy dispersive spectroscopy*

Scanning electron microscopy (SEM) can be described as a microscopy technique which involves directing a beam of electrons at a target specimen in order to map its surface morphology. The interaction of the electron beam with the specimen generates several secondary emissions. SEM provides high resolution images with a long depth of field and can be utilised with energy dispersive spectroscopy detectors. Energy dispersive spectroscopy (EDS) provides chemical and elemental analyses of specimens inside the SEM.

For the SEM analysis conducted in this investigation, an accelerating voltage of 15kV was applied to the specimens in order to minimise the potential damage to the polymer membrane. Oxford Instrument's Aztec Live software was used for the EDS analysis of the specimens. The MEA specimens were characterised from a cross-sectional orientation.

shows the SEM image of the 2mg cm^{-2} Pt-Ru MEA.

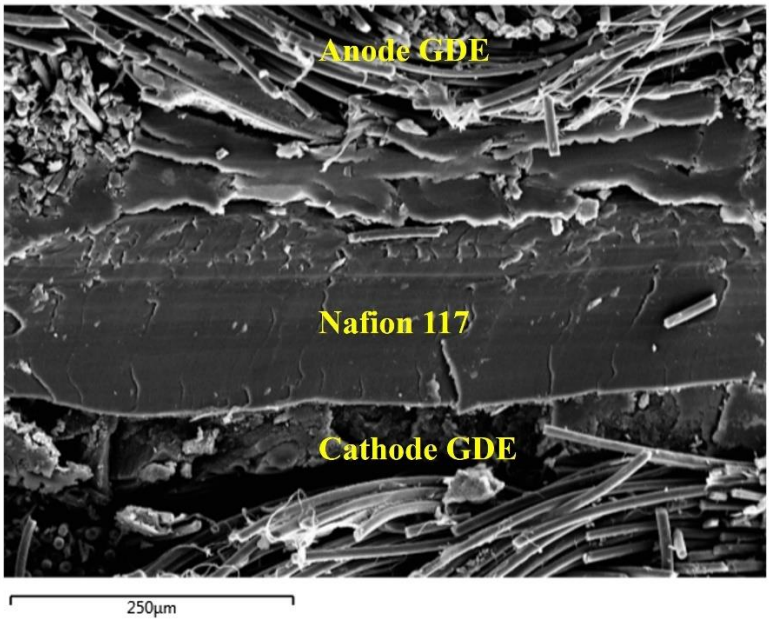

Figure 12. SEM image of 2 $mg_{Pt\text{-}Ru}$ cm^{-2} MEA

In

, the polymer membrane is the thick material layer in the centre of the image spanning across the horizontal plane. The anode and cathode catalyst layers are the thin layers that can be seen on the lower and upper sides of the membrane respectively. The carbon cloth gas diffusion layers are the interwoven fibrous layers seen above and below each side of the catalyst layers.

shows the elemental composition from the EDS analysis of the 2.0 mg cm^{-2} Pt-Ru MEA.

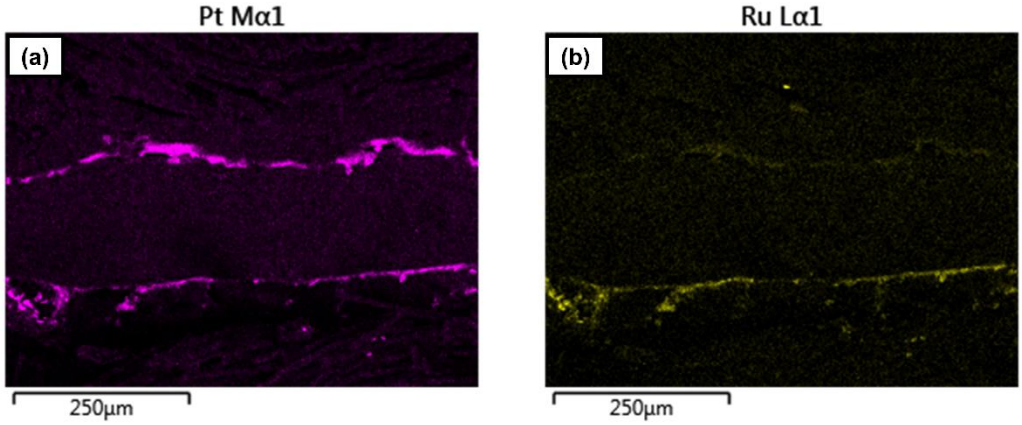

Figure 13. Elemental composition of 2$mg_{Pt\text{-}Ru}$ cm^{-2} MEA from EDS analysis (a) Pt and (b) Ru

In

(a), sufficient Pt deposition can be observed on both the anode and cathode catalyst layers with adequate distribution uniformity across each of the layers. The elemental composition for Ru also showed satisfactory deposition and distribution across the anode catalyst layer (Fig. 13 (b)). These results provide a suitable frame of reference for comparison with the novel catalyst MEA's.

shows the SEM image and elemental composition from the EDS analysis of the novel catalyst (Pt-$NiTiO_3$) MEA with a loading of 0.5 mg cm^{-2}.

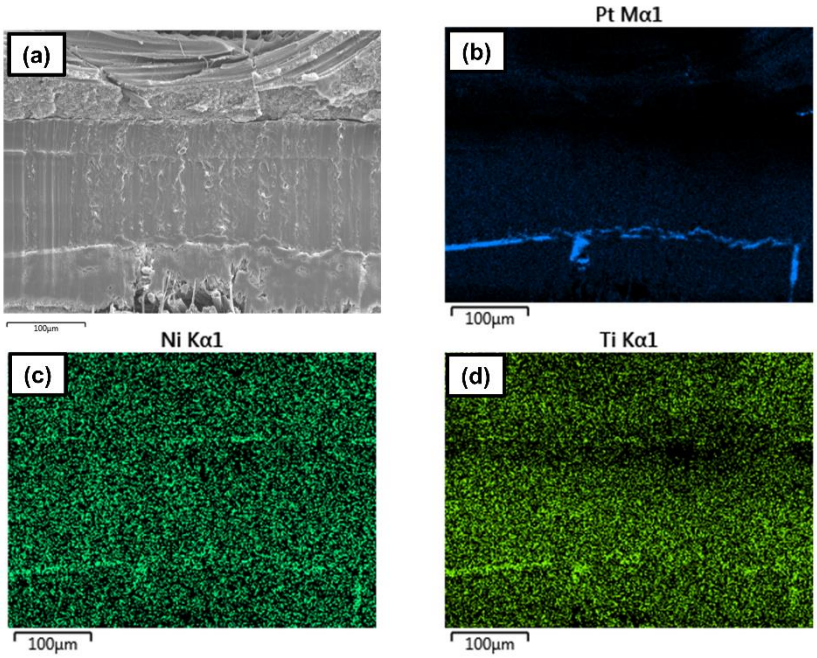

Figure 14. SEM and EDS analysis of MEA with novel Pt-$NiTiO_3$ catalyst on anode. (a) Cross sectional view of MEA, (b) Pt, (c) Ni and (d) Ti

In

(a), the commercial cathode catalyst layer is situated on the upper side of the membrane and the novel anode catalyst layer is situated on the lower side of the membrane. In Fig. 14 (b) of Pt, it can be observed that the anode catalyst layer has a very good Pt distribution across the entire catalyst layer. Conversely, the commercial catalyst layer appears to be completely devoid of any catalyst deposition with only one region displaying a small cluster of Pt. It has been suggested that this could be due to a number of reasons such as poor fabrication quality of the catalyst ink and catalyst coating or the occurrence of delamination of the catalyst layer from the membrane leading to catalyst dissolution. The Ni and Ti EDS images (Fig. 14. (c) & (d)) contain a significant amount of noise so is difficult to observe the overall elemental distribution, but a faint deposition layer can be seen on the left side of the anode. The SEM and EDS analyses help to reveal that the absence of Pt on the cathode catalyst layer resulted in the poor performance observed in the polarisation curves in

. However, the high quality of Pt deposition and distribution on the anode catalyst layer is promising for further testing at the stack level. The next stage in experimental work progressed to testing a $100cm^2$ 3-cell stack using the novel Pt-$NiTiO_3$ catalyst.

5.3 *$100cm^2$ 3-cell stack*

5.3.1 *Test conditions*

Table 6 outlines the conditions used for experimental testing of the $100cm^2$ 3 cell stack.

Table 6. Testing conditions for $100cm^2$ 3-cell stack

Parameter		Value
Anode flow	Methanol concentration	1.0 M
	Flow rate	12 ml min^{-1}
	Temperature	40 °C
Cathode flow	Reactant	Air
	Flow rate	4000 ml min^{-1}
	Temperature	65 °C

	Humidity	100% RH
Other	Stack temperature	70 °C

5.3.2 *Polarization*

In the third stage of testing, 100cm^2 MEAs were fabricated in order to investigate the feasibility of the coating technique and performance of Pt-$NiTiO_3$/C catalyst in a 3-cell stack. Fig. 14 shows the polarization results from stack testing.

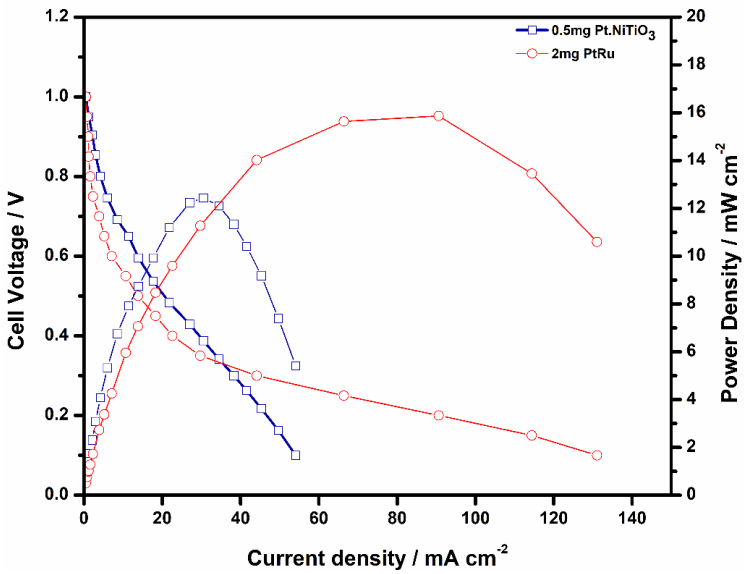

Figure 15. Polarization and Power Density curve of 3-cell DMFC stack (100cm^2 MEAs)

The OCV achieved by the Pt-$NiTiO_3$ stack was measured at 0.951V which is equates to 0.317V per cell. This result reveals there is a voltage loss of 18mV per cell compared to the single Pt-$NiTiO_3$ MEA which produced an OCV of 0.335V. Given the relatively low catalyst loading of 0.5 mg cm^{-2} Pt-$NiTiO_3$ (0.33 mgPt cm^{-2}), an OCV of 0.95V indicates moderate performance. However, these OCV results from 100cm^2 Pt-$NiTiO_3$ MEAs are considerably lower than the 25cm^2 Pt-$NiTiO_3$ MEAs which achieved between 0.45V-0.47V at OCV for catalyst loadings of 0.29 mgPt cm^{-2} and 0.66 mgPt cm^{-2} respectively. This suggests that the catalyst coating technique may not be the optimal technique for large scale MEAs and may require other techniques to be investigated in future research. The peak current density achieved by the Pt-$NiTiO_3$ 3-cell stack was 53.36 mA cm^{-2} which demonstrated an increase of 8.21 mA cm^{-2} compared to the peak current density achieved by the Pt-$NiTiO_3$ single MEA of 45.15mA. In order to fully characterise the performance of the Pt-$NiTiO_3$ catalyst and coating technique for large scale MEAs and at stack level, future work should investigate using additional electrochemical characterisation techniques and compare results with a stack comprised of commercial Pt-Ru MEAs with equivalent catalyst loading.

5.3.3 *Peak power*

Peak power density was compared between the Pt-$NiTiO_3$ stack, Pt-Ru MEA. Fig. 15 shows the comparison of power density curves.

The peak power densities achieved were 12.1 mW cm^{-2} and 12.7 mW cm^{-2}, for the Pt-$NiTiO_3$ stack and Pt-Ru MEA respectively. This demonstrates that the 0.5 mg cm^{-2} Pt-$NiTiO_3$ catalyst was able to achieve approx. the same peak power density as the commercial 2 mg cm^{-2} Pt-Ru catalyst. The limited peak current density of the Pt-$NiTiO_3$ stack could be due to the lower catalyst loading or highlight the need for improved flow distribution at the stack level. Nevertheless, the results from this feasibility study demonstrate good performance of the Pt-$NiTiO_3$ catalyst in terms of peak power density in a 100cm^2 3-cell stack considering the low Pt loading. This shows potential for further investigations in two main areas including stack testing with equal catalyst loadings to enable more accurate performance comparisons (e.g. 1.0 mg cm^{-2}) and to identify an optimal catalyst loading of Pt-$NiTiO_3$ by determining the point of diminishing returns of performance.

5.3.4 *Scanning electron microscopy and energy dispersive spectroscopy*

Fig.16 shows the SEM and EDS analyses from a sample of the novel catalyst (Pt-$NiTiO_3$) MEA taken from the 3-cell stack. The anode and cathode catalyst layers are on the lower and upper side of the membrane respectively.

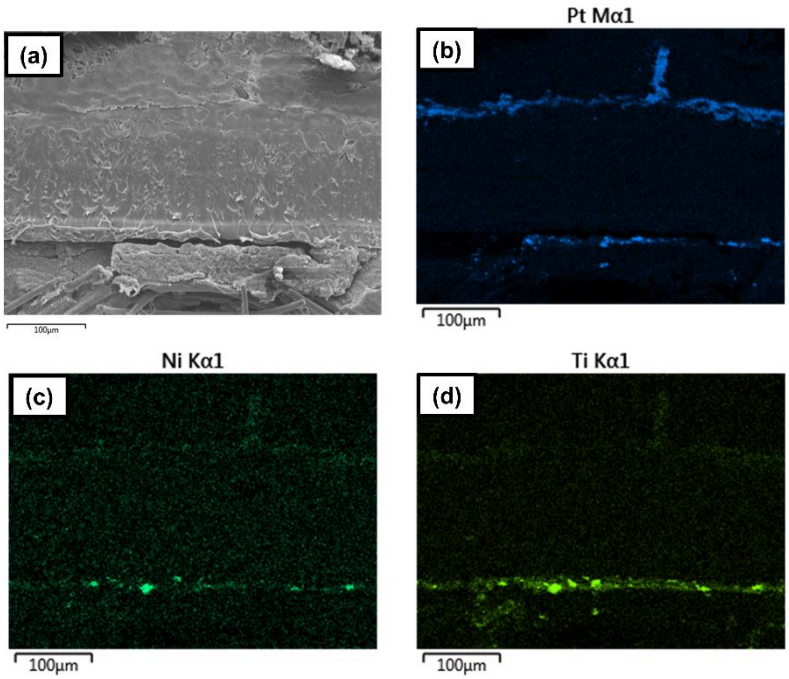

Figure 16. SEM and EDS analysis of novel Pt-$NiTiO_3$ anode catalyst from 3-cell stack. (a) Cross sectional view of MEA, (b) Pt, (c) Ni and (d) Ti

In **Error! Reference source not found.**6 (a), the EDS image of Pt shows that the commercial cathode catalyst has a satisfactory deposition and uniform distribution across the whole catalyst layer. The novel anode catalyst layer appears to have adequate Pt catalyst deposition and distribution across the majority of the catalyst layer although one region has minimal Pt deposition (Fig. 16. (b)). The apparent deficiency of Pt in this area could be attributed to minor damage to the specimen the during sample preparation. This can be observed in the lower left-hand corner of the SEM image on the cross-sectional surface area of the anode catalyst layer and would explain some of the loss of material including the Pt catalyst. For the Ni and Ti elemental compositions, the EDS imaging (Fig. 16. (c) & (d)) shows satisfactory deposition and distribution across the anode catalyst layer, although clusters of elemental particles can be observed, and a noticeable deficiency is evident in the same left hand side region. In comparison to the EDS analysis of the single cell Pt-$NiTiO_3$ MEA, the specimen from the Pt-$NiTiO_3$ 3-cell stack revealed that satisfactory catalyst deposition and distribution was achieved on both the anode and cathode catalyst layers which supports the polarisation curve results as the 3-cell stack achieved higher current and power densities. Further work should aim to conduct experimental testing on a 3-cell stack with commercial Pt-Ru anode catalyst for comparison.

6. Conclusions

The impact of anode platinum loading on the performance of DMFC was investigated, employing cells equipped with both Pt-$NiTiO_3$ and Pt-Ru based anode electrocatalysts. The findings demonstrated a consistent performance improvement with increasing anode platinum loading for the Pt-$NiTiO_3$ catalyst. Conversely, for Pt-Ru based catalysts, an optimal point was identified at 0.66 mg_{Pt} cm^{-2}. Adhering to this loading limit for the catalyst can contribute to reducing the material cost of the membrane electrode assembly. To further explore this, additional investigations using alternative catalyst ink coating techniques should be conducted to reliably achieve higher anode platinum loadings with the innovative Pt-$NiTiO_3$ catalyst. This exploration should encompass determining the point of diminishing performance returns for small-scale (25 cm^2) MEAs, followed by large-scale (100 cm^2) MEAs and progressing to stacks.

Acknowledgments

The authors would like to acknowledge the support of the joint UKIERI-DST project on "Methanol Fed High Energy Density Fuel Cell Systems with Novel Catalyst and Flow Field Design" (DST-UKIERI-2016-17-0023).

Conflict of interest

There is no conflict of interest for this study.

References

[1] Shin, D.W.; Guiver, M.D.; Lee, Y.M. Hydrocarbon-Based Polymer Electrolyte Membranes: Importance of Morphology on Ion Transport and Membrane Stability. *Chem. Rev.* **2017**, *117*, 4759–4805, https://doi.org/10.1021/acs.chemrev.6b00586.

[2] Kusoglu, A.; Weber, A.Z. New Insights into Perfluorinated Sulfonic-Acid Ionomers. *Chem. Rev.* **2017**, *117*, 987–1104, https://doi.org/10.1021/acs.chemrev.6b00159.

[3] Zhao, X.; Yin, M.; Ma, L.; Liang, L.; Liu, C.; Liao, J.; Lu, T.; Xing, W. Recent advances in catalysts for direct methanol fuel cells. *Energy Environ. Sci.* **2011**, *4*, 2736–2753, https://doi.org/10.1039/c1ee01307f.

[4] Liu, G.; Ding, X.; Zhou, H.; Chen, M.; Wang, M.; Zhao, Z.; Yin, Z.; Wang, X. Structure optimization of cathode microporous layer for direct methanol fuel cells. *Appl. Energy* **2015**, *147*, 396–401, https://doi.org/10.1016/j.apenergy.2015.03.021.

[5] Holton O, Stevenson J. The Role of Platinum in Proton Exchange Membrane Fuel Cells - Johnson Matthey Technology Review. Platin Met Rev 2013;57:259–71.

[6] Ahmed, M.; Dincer, I. A review on methanol crossover in direct methanol fuel cells: challenges and achievements. *Int. J. Energy Res.* **2011**, *35*, 1213–1228, https://doi.org/10.1002/er.1889.

[7] Seo, S.H.; Lee, C.S. A study on the overall efficiency of direct methanol fuel cell by methanol crossover current. *Appl. Energy* **2010**, *87*, 2597–2604, https://doi.org/10.1016/j.apenergy.2010.01.018.

[8] Mondal, S.; Malik, S. Easy synthesis approach of Pt-nanoparticles on polyaniline surface: an efficient electro-catalyst for methanol oxidation reaction. *J. Power Sources* **2016**, *328*, 271–279, https://doi.org/10.1016/j.jpowsour.2016.08.026.

[9] Wu, G.; Li, L.; Xu, B.-Q. Effect of electrochemical polarization of PtRu/C catalysts on methanol electrooxidation. *Electrochimica Acta* **2004**, *50*, 1–10, https://doi.org/10.1016/j.electacta.2004.07.006.

[10] Ruiz-Camacho, B.; Martínez-González, J.; González-Huerta, R.; Tufiño-Velázquez, M. Kinetic study of oxygen reduction reaction and PEM fuel cell performance of Pt/TiO 2 -C electrocatalyst. *Int. J. Hydrogen Energy* **2014**, *39*, 16731–16739, https://doi.org/10.1016/j.ijhydene.2014.02.109.

[11] Alia, S.M.; Jensen, K.; Contreras, C.; Garzon, F.; Pivovar, B.; Yan, Y. Platinum Coated Copper Nanowires and Platinum Nanotubes as Oxygen Reduction Electrocatalysts. *ACS Catal.* **2013**, *3*, 358–362, https://doi.org/10.1021/cs300664g.

[12] Moura, A.S.; Fajín, J.L.C.; Mandado, M.; Cordeiro, M.N.D.S. Ruthenium–Platinum Catalysts and Direct Methanol Fuel Cells (DMFC): A Review of Theoretical and Experimental Breakthroughs. *Catalysts* **2017**, *7*, 47, https://doi.org/10.3390/catal7020047.

[13] Igarashi, H.; Uchida, H.; Suzuki, M.; Sasaki, Y.; Watanabe, M. Removal of carbon monoxide from hydrogen-rich fuels by selective oxidation over platinum catalyst supported on zeolite. *Appl. Catal. A: Gen.* **1997**, *159*, 159–169, https://doi.org/10.1016/s0926-860x(97)00075-6.

[14] Kahlich, M.; Gasteiger, H.; Behm, R. Kinetics of the Selective CO Oxidation in H2-Rich Gas on Pt/Al2O3. *J. Catal.* **1997**, *171*, 93–105, https://doi.org/10.1006/jcat.1997.1781.

[15] Andrew Hamnett. Mechanism of Methanol Electro-Oxidation. Interface Electrochem., 1999, p. 41.

[16] Akhairi, M.A.F.; Kamarudin, S.K. Catalysts in direct ethanol fuel cell (DEFC): An overview. *Int. J. Hydrog. Energy* **2016**, *41*, 4214–4228, https://doi.org/10.1016/j.ijhydene.2015.12.145.

[17] Wang, L.; Yuan, Z.; Wen, F.; Cheng, Y.; Zhang, Y.; Wang, G. A bipolar passive DMFC stack for portable applications. *Energy* **2017**, *144*, 587–593, https://doi.org/10.1016/j.energy.2017.12.039.

[18] Nakagawa, N.; Tsujiguchi, T.; Sakurai, S.; Aoki, R. Performance of an active direct methanol fuel cell fed with neat methanol. *J. Power Sources* **2012**, *219*, 325–332, https://doi.org/10.1016/j.jpowsour.2012.07.062.

[19] Liu, J.; Zhao, T.; Chen, R.; Wong, C. The effect of methanol concentration on the performance of a passive DMFC. *Electrochem. Commun.* **2005**, *7*, 288–294, https://doi.org/10.1016/j.elecom.2005.01.011.

[20] Qi, Z.; Kaufman, A. Open circuit voltage and methanol crossover in DMFCs. *J. Power Sources* **2002**, *110*, 177–185, https://doi.org/10.1016/s0378-7753(02)00268-9.
[21] Copper, C.L.; Koubek, E.; Cermak; Wiemer; Copper; Koubek; Monk; Mohan; Sponholtz; Walters; et al. An Experiment to Demonstrate How a Catalyst Affects the Rate of a Reaction. *J. Chem. Educ.* **1999**, *76*, https://doi.org/10.1021/ed076p1714.
[22] Ercelik, M.; Ozden, A.; Seker, E.; Colpan, C.O. Characterization and performance evaluation of Pt Ru/C TiO2 anode electrocatalyst for DMFC applications. *Int. J. Hydrogen Energy* **2017**, *42*, 21518–21529, https://doi.org/10.1016/j.ijhydene.2016.12.020.
[23] Fathirad, F.; Mostafavi, A.; Afzali, D. Bimetallic Pd–Mo nanoalloys supported on Vulcan XC-72R carbon as anode catalysts for direct alcohol fuel cell. *Int. J. Hydrogen Energy* **2017**, *42*, 3215–3221, https://doi.org/10.1016/j.ijhydene.2016.09.138.
[24] Sharma, S.; Pollet, B.G. Support materials for PEMFC and DMFC electrocatalysts—A review. *J. Power Sources* **2012**, *208*, 96–119, https://doi.org/10.1016/j.jpowsour.2012.02.011.
[25] Patel, P.P.; Datta, M.K.; Jampani, P.H.; Hong, D.; Poston, J.A.; Manivannan, A.; Kumta, P.N. High performance and durable nanostructured TiN supported Pt50–Ru50 anode catalyst for direct methanol fuel cell (DMFC). *J. Power Sources* **2015**, *293*, 437–446, https://doi.org/10.1016/j.jpowsour.2015.05.051.
[26] Liu, H.; Song, C.; Zhang, L.; Zhang, J.; Wang, H.; Wilkinson, D.P. A review of anode catalysis in the direct methanol fuel cell. *J. Power Sources* **2006**, *155*, 95–110, https://doi.org/10.1016/j.jpowsour.2006.01.030.
[27] Antolini E. Platinum Alloys as Anode Catalysts for Direct Methanol Fuel Cells. Electrocatal Direct Methanol Fuel Cells From Fundam to Appl 2009:227–55. https://doi.org/10.1002/9783527627707.ch6.
[28] Frelink, T.; Visscher, W.; van Veen, J. On the role of Ru and Sn as promotors of methanol electro-oxidation over Pt. *Surf. Sci.* **1995**, *335*, 353–360, https://doi.org/10.1016/0039-6028(95)00412-2.
[29] Li, Y.; Bastakoti, B.P.; Malgras, V.; Li, C.; Tang, J.; Kim, J.H.; Yamauchi, Y. Polymeric Micelle Assembly for the Smart Synthesis of Mesoporous Platinum Nanospheres with Tunable Pore Sizes. *Angew. Chem. Int. Ed.* **2015**, *54*, 11073–11077, https://doi.org/10.1002/anie.201505232.
[30] Li, C.; Yamauchi, Y. Facile solution synthesis of Ag@Pt core–shell nanoparticles with dendritic Pt shells. *Phys. Chem. Chem. Phys.* **2013**, *15*, 3490–3496, https://doi.org/10.1039/c3cp44313b.
[31] Abdelkareem, M.A.; Ito, Y.; Tsujiguchi, T.; Nakagawa, N. Carbon-TiO_2 Composite Nanofibers as a Promising Support for PtRu Anode Catalyst of DMFC. *ECS Trans.* **2013**, *50*, 1959–1967, https://doi.org/10.1149/05002.1959ecst.
[32] Shan, C.-C.; Tsai, D.-S.; Huang, Y.-S.; Jian, S.-H.; Cheng, C.-L. Pt−Ir−IrO_2NT Thin-Wall Electrocatalysts Derived from IrO_2 Nanotubes and Their Catalytic Activities in Methanol Oxidation. *Chem. Mater.* **2007**, *19*, 424–431, https://doi.org/10.1021/cm062085u.
[33] Zhang, Y.; Zhang, H.; Ma, Y.; Cheng, J.; Zhong, H.; Song, S.; Ma, H. A novel bifunctional electrocatalyst for unitized regenerative fuel cell. *J. Power Sources* **2009**, *195*, 142–145, https://doi.org/10.1016/j.jpowsour.2009.07.018.
[34] Scibioh, M.A.; Kim, S.-K.; Cho, E.A.; Lim, T.-H.; Hong, S.-A.; Ha, H.Y. Pt-CeO2/C anode catalyst for direct methanol fuel cells. *Appl. Catal. B: Environ.* **2008**, *84*, 773–782, https://doi.org/10.1016/j.apcatb.2008.06.017.
[35] Maiyalagan, T.; Khan, F.N. Electrochemical oxidation of methanol on Pt/V2O5–C composite catalysts. *Catal. Commun.* **2009**, *10*, 433–436, https://doi.org/10.1016/j.catcom.2008.10.011.
[36] Micoud, F.; Maillard, F.; Gourgaud, A.; Chatenet, M. Unique CO-tolerance of Pt–WOx materials. *Electrochem. Commun.* **2009**, *11*, 651–654, https://doi.org/10.1016/j.elecom.2009.01.007.
[37] Justin, P.; Rao, G.R. Methanol oxidation on MoO3 promoted Pt/C electrocatalyst. *Int. J. Hydrogen Energy* **2011**, *36*, 5875–5884, https://doi.org/10.1016/j.ijhydene.2011.01.122.
[38] Thiagarajan, V.; Manoharan, R.; Karthikeyan, P.; Nikhila, E.; Hernández-Ramírez, A.; Rodriguez-Varela, F. Pt nanoparticles supported on NiTiO3/C as electrocatalyst towards high performance Methanol Oxidation Reaction. *Int. J. Hydrogen Energy* **2017**, *42*, 9795–9805, https://doi.org/10.1016/j.ijhydene.2017.01.017.
[39] Vijayalakshmi, R.; Rajendran, V. Effect of Reaction Temperature on Size and Optical Properties of $NiTiO_3$Nanoparticles. *E-Journal Chem.* **2012**, *9*, 282–288, https://doi.org/10.1155/2012/607289.
[40] Chellasamy, V.; Thangadurai, P. Structural and electrochemical investigations of nanostructured NiTiO3 in acidic environment. *Front. Mater. Sci.* **2017**, *11*, 162–170, https://doi.org/10.1007/s11706-017-0380-1.
[41] Flórez-Montaño, J.; Calderón-Cárdenas, A.; Lizcano-Valbuena, W.; Rodríguez, J.L.; Pastor, E. Ni@Pt nanodisks with low Pt content supported on reduced graphene oxide for methanol electrooxidation in alkaline media. *Int. J. Hydrogen Energy* **2016**, *41*, 19799–19809, https://doi.org/10.1016/j.ijhydene.2016.06.166.
[42] Amin, R.; Hameed, R.A.; El-Khatib, K.; Youssef, M.E. Electrocatalytic activity of nanostructured Ni and Pd–Ni on Vulcan XC-72R carbon black for methanol oxidation in alkaline medium. *Int. J. Hydrogen Energy* **2014**, *39*, 2026–2041, https://doi.org/10.1016/j.ijhydene.2013.11.033.

[43] Mancharan, R.; Goodenough, J.B. Methanol oxidation in acid on ordered NiTi. *J. Mater. Chem.* **1992**, *2*, 875–887, https://doi.org/10.1039/jm9920200875.
[44] Thiagarajan, V.; Karthikeyan, P.; Thanarajan, K.; Neelakrishnan, S.; Manoharan, R.; Chen, R.; Fly, A.; Anand, R.; Raj, T.R.K.; Kumar, N.S. Experimental investigation on DMFCs using reduced noble metal loading with NiTiO3 as supportive material to enhance cell performances. *Int. J. Hydrogen Energy* **2019**, *44*, 13415–13423, https://doi.org/10.1016/j.ijhydene.2019.03.244.
[45] Thiagarajan, V.; Karthikeyan, P.; Manoharan, R.; Sampath, S.; Hernández-Ramírez, A.; Sánchez-Castro, M.; Alonso-Lemus, I.; Rodríguez-Varela, F. Pt-Ru-NiTiO3 Nanoparticles Dispersed on Vulcan as High Performance Electrocatalysts for the Methanol Oxidation Reaction (MOR). *Electrocatalysis* **2018**, *9*, 582–592, https://doi.org/10.1007/s12678-017-0450-2.
[46] Lin, Y.; Cui, X.; Yen, C.H.; Wai, C.M. PtRu/Carbon Nanotube Nanocomposite Synthesized in Supercritical Fluid: A Novel Electrocatalyst for Direct Methanol Fuel Cells. *Langmuir* **2005**, *21*, 11474–11479, https://doi.org/10.1021/la051272o.
[47] Kumaresan, T.; Velumani, T.; Chandran, M.; Palaniswamy, K.; Thirkell, A.; Fly, A.; Chen, R.; Sundaram, S. Effect of Nafion loading and the novel flow field designs on innovative anode electrocatalyst for improved Direct Methanol Fuel cells performance. *Mater. Lett.* **2020**, *276*, https://doi.org/10.1016/j.matlet.2020.128222.
[48] Gancs, L.; Hakim, N.; Hult, B.; Mukerjee, S. Dissolution of Ru from PtRu Electrocatalysts and its Consequences in DMFCs. *ECS Trans.* **2006**, *3*, 607–618, https://doi.org/10.1149/1.2356181.
[49] Piela, P.; Eickes, C.; Brosha, E.; Garzon, F.; Zelenay, P. Ruthenium Crossover in Direct Methanol Fuel Cell with Pt-Ru Black Anode. *J. Electrochem. Soc.* **2004**, *151*, A2053–A2059, https://doi.org/10.1149/1.1814472.
[50] Su, K.; Yao, X.; Sui, S.; Wei, Z.; Zhang, J.; Du, S. Ionomer content effects on the electrocatalyst layer with in-situ grown Pt nanowires in PEMFCs. *Int. J. Hydrogen Energy* **2014**, *39*, 3219–3225, https://doi.org/10.1016/j.ijhydene.2013.12.117.
[51] Ngo, T.T.; Yu, T.L.; Lin, H.-L. Influence of the composition of isopropyl alcohol/water mixture solvents in catalyst ink solutions on proton exchange membrane fuel cell performance. *J. Power Sources* **2013**, *225*, 293–303, https://doi.org/10.1016/j.jpowsour.2012.10.055.
[52] Inoue, M.; Iwasaki, T.; Sayama, K.; Umeda, M. Effect of conditioning method on direct methanol fuel cell performance. *J. Power Sources* **2010**, *195*, 5986–5989, https://doi.org/10.1016/j.jpowsour.2009.11.015.
[53] Han, J.; Liu, H. Real time measurements of methanol crossover in a DMFC. *J. Power Sources* **2006**, *164*, 166–173, https://doi.org/10.1016/j.jpowsour.2006.09.105.
[54] Arumughan, J.; Vijayakrishnan, M.K.; Palaniswamy, K.; Alam, T.; Kumaresan, T.; Angappamudaliar, S.K.P.; Sundaram, S. Electrochemical analysis of nano-electro fuels based on multi-walled carbon nanotubes and graphene nanoplatelets for vanadium redox flow batteries. *Mater. Lett.* **2022**, *315*, https://doi.org/10.1016/j.matlet.2022.131939.
[55] Marappan, M.; Arumughan, J.; Manoharan, K.; Kumaresan, T.; Vijayakrishnan, M.K.; Palaniswamy, K. Experimental investigation on serpentine, parallel and novel zig-zag flow fields for effective water removal and enhanced performance on 25 cm2 PEMFC. **2021**, https://doi.org/10.36410/jcpr.2021.22.2.131.